1
2 *In situ* estimates of iron-oxidation and accretion rates for iron-oxidizing bacterial mats at
3 Lō'ihi Seamount.
4
5
6
7
8
9
10
11
12
13
14
15 David Emerson[1][*], Jarrod J. Scott[1], Anna Leavitt[1], Emily Fleming[2], Craig Moyer[3].
16
17
18 [1]Bigelow Laboratory for Ocean Sciences, East Boothbay, ME; [2]California State
19 University, Chico, CA; [3]Western Washington University, Bellingham, WA
20
21
22
23
24 *Corresponding author:
25 Bigelow Laboratory for Ocean Sciences, 60 Bigelow Dr, East Boothbay, ME 04544;
26 demerson@bigelow.org; (207)315-2567
27
28
29
30
31 12 December, 2016
32
33
34

35
36   Highlights.
37
38   • An *in-situ* productivity chamber was developed to estimate rates of Fe-oxidation and
39   understand colonization patterns at chemosynthetic iron mats at Lō'ihi Seamount.
40
41   • Fe-oxidation rates ranged from 8.2–51.9 x 10^{-6} mol $\cdot$ hr^{-1}, and it was estimated that the
42   iron mats could accrete at around 2.2 cm $\cdot$ yr^{-1}.
43
44   • The iron mat community was dominated by Zetaproteobacteria, whose relative
45   abundance accounted for up to 89% of the microbial community.
46
47   • The community membership that grew during short-term incubations reflected the
48   community composition of nearby microbial mats.
49
50
51

52 **Abstract.**

53

54   It is increasingly recognized that diffuse, hydrothermal venting is an important source of

55   iron to the deep-sea that can influence oceanic iron dynamics and abundance.

56   Lithotrophic Fe-oxidizing bacteria (FeOB) are dominant at diffuse hydrothermal vent

57   sites, producing microbial iron mats that are often centimeters or more thick. At present,

58   little is known about *in situ* Fe-oxidation rates, or accretion rates for iron mats. An *in situ*

59   productivity chamber was developed that took advantage of the unique mineral

60   morphotypes produced by FeOB to estimate rates of Fe-oxidation and accretion.

61   Chambers were placed at two diffuse vents (1179 and 1300 mbsl) at Lō'ihi Seamount

62   where they were colonized by FeOB for different amounts of time. From this analysis, it

63   was estimated that Fe-oxidation rates could range from 8.2–51.9 x 10^{-6} mol $\cdot$ hr^{-1}, and that

64   iron mats could accrete at around 2.2 cm $\cdot$ yr^{-1}. Molecular analysis indicated that the

65   relative abundance of Zetaproteobacteria, a group of known FeOB, accounted for 80–

66   90% of the bacteria colonizing the chambers. There was a distinct difference between

67   populations at the 1179m site (Pohaku), and the 1300m site (North Hiolo Ridge).

68   Microscope slides placed within the productivity chambers were colonized by different

69   morphotypes of FeOB. The cells responsible for one common morphotype that produces

70   a Y-shaped filament were identified as Zetaproteobacteria by use of a small subunit

71   rRNA probe. This work confirms the importance of FeOB in the formation of

72   chemosynthetic iron mats, and provides the first estimates for *in situ* Fe-oxidation rates

73   and mat accretion rates.

74   **1. Introduction.**

75

76   Many marine hydrothermal vent systems host chemosynthetic microbial mat

77   communities dominated by lithotrophic Fe-oxidizing bacteria (FeOB) that live on Fe(II)-

78   rich, anoxic fluids emanating from the seafloor. These vent ecosystems are found both in

79   the deep-sea and in shallow waters, and can be associated with active volcanic

80   seamounts, as well as tectonic crustal spreading and subduction zones (Boothman and

81   Lloyd, 2010; Emerson and Moyer, 2002; Kato et al., 2009; Scott et al., 2015). The most

82   active Fe-oxidizing communities are associated with cooler, diffuse flow systems capable

83   of supporting microbial mats that are often centimeters thick or more. Despite numerous

84   studies of microbial iron mats, the *in situ* activities marine of FeOB are not well studied,

85   nor do we know the accretion rates of *in situ* iron mats. The rapid heterogeneous

86   oxidation (also referred to as auto-oxidation) of iron at circumneutral pH make it

87   challenging to distinguish between abiotic and biotic reactions, thus making simple mass

88   balance calculations difficult to interpret (Melton et al., 2014). Iron isotopes have proven

89   useful for distinguishing some types of abiotic from biotic oxidation of iron, but are less

90   suitable for specific rate measurements (Johnson et al., 2008). Thus there are inherent

91   challenges to assessing the *in situ* activity of Fe-oxidizing microbial communities.

92   A more detailed understanding of the productivity of these Fe-fueled ecosystems

93   can also help better constrain their contribution to the oceanic Fe budget. It is clear there

94   are still significant unknowns regarding the contribution of hydrothermal sources of iron

95   to the ocean's iron budget (German et al., 2015; Resing et al., 2015). Furthermore, the

96   biogenic iron oxides produced at hydrothermal vents have unique properties. They are

97   often referred to as hydrous ferric oxides (HFO) in part because they are poorly

98   crystalline oxides, composed primarily of ferrihydrite, with large surface areas that

99   adsorb water and are relatively buoyant (Emerson, 2016). These biogenic oxides undergo

100   diagenesis to crystalline forms more slowly than synthesized iron oxides, probably as a

101   result of containing organic ligands, as well as becoming silicified (Kennedy et al., 2004;

102   Picard et al., 2015; Toner et al., 2012). Combined, these properties of biogenic iron

103   oxides may result in longer residence times in the water column, and increased

104   bioavailability.   There is evidence that biogenic iron oxides contribute to the iron flux

105   into the ocean (Bennett et al., 2011; Toner et al., 2009), thus understanding details about

106   their production is important to understanding their contribution as a global iron source.

107   One avenue for assessing *in situ* activity, and estimating iron oxidation rates is to

108   take advantage of the unique morphotypes of biogenic oxides produced by FeOB. These

109   morphotypes include cylindrical filamentous sheaths, helical stalks, short tubular stalks

110   (referred to here as Y's), and other filamentous forms (Chan et al., 2016). Freshly

111   produced biogenic morphotypes are relatively easy to classify by light microscopy, thus

112   FeOB offer a rare opportunity to observe microbial growth in nature. We chose to utilize

113   this approach, hypothesizing that use of a chamber designed to capture iron oxides and

114   cell morphologies could provide insight into how FeOB colonization may occur, further

115   our understanding of the population dynamics involved in colonization, and provide an

116   estimate for *in-situ* growth rates.

117

118   **2. Materials and Methods.**

119   *2.1 Chamber Design.* A productivity chamber was designed for seafloor deployment. The

120   chamber consisted of a central open rectangular section that held microscope slides and

121   weights (Fig. 1). The microscope slides were placed in standard 50 ml conical tubes (1

122   slide/tube) with the bottoms removed. A zip-tie was attached at the top and bottom of the

123   tube to prevent the slides from falling out. The conical tubes were then attached to the

124   open interior of the chamber with zip-ties. A hollow tube, referred to here as a cassette,

125   with open screw-cap ends that had Nitex nylon mesh cut to fit the openings on either end

126   was strapped on either side of the chamber with zip ties, as shown in Fig.1. The volume

127   each cassette was 95 ml. The chamber and cassette was constructed from PVC hardware

128   purchased at a building supply store. To allow for manipulation by the robotic arm of a

129   submersible, a lanyard of floating polypropylene line with a small float of syntactic foam

130   was attached to each chamber.

131

132   *2.2 Chamber Deployment and recovery.* Chambers were deployed at two sites on the

133   seafloor in close vicinity to diffuse flow hydrothermal vents at Lō'ihi Seamount

134   (18.920°N, 155.270°W). Deployment was done using the ROV *Jason 2* during the initial

135   dives of a 14 day expedition to Lō'ihi in spring of 2013. The first deployment of 4

136   chambers (8 cassettes) was at Pohaku vents (sometimes referred to as Marker 57) at a

137   depth of 1,179m. The second deployment of four chambers was at North Hiolo Ridge

138   (NHR, Marker 39) at a depth of 1300m. Chambers were inspected on 'fly-bys' during

139   subsequent submersible operations to visually assess if iron oxides were accumulating in

140   the cassettes. At Pohaku, due to a lack of iron-oxide accumulation, the chambers were re-

141   deployed after 7 days, as described in the Results and Discussion section. Miniature

142   temperature recorders (MTRs) were deployed in vents at both the NHR and Pohaku sites.

143   For recovery, the chambers were placed in a closed bio-box mounted on the

144   submersible to maintain static water conditions during subsequent ROV operations. As

145   soon as *Jason* was on deck, the bio-box was opened, and while still submerged rubber

146   stoppers (size 9 1/2) were pushed into the bottom opening of the cassettes to prevent the

147   water entrained in them from draining out after the chambers were removed from the bio-

148   box. In the lab the cassettes were removed from the chamber body, and the top mesh

149   removed. The iron oxides that accumulated in the cassette were placed in sterile 50 ml

150   conical tubes with a 25 ml pipette. These oxides were processed for analysis of cell

151   counts, morphology, and total iron, and a subsample was frozen for DNA extraction. The

152   microscope slides from the chamber interior were removed and air-dried. Perhaps as a

153   result of the longer incubation times at NHR, the individual cassettes for each chamber

154   contained more oxides than the Pohaku chambers. For this reason, each cassette from the

155   NHR chambers was harvested separately, while the two cassettes for each of the four

156   Pohaku samples were combined to a single sample. As a result, the oxidation rates

157   reported in Table 1 are broken into the individual cassettes for NHR samples, but

158   combined for the cassettes from the Pohaku chambers.

159

160   *2.3 Cell counts.* Cell counts were done on aliquots of the iron oxides that were fixed in

161   2% glutaraldehyde. Counting was done by diluting the original sample between 1:2 and

162   1:5, depending upon the initial cell density, and then using 10 µl of the diluted material to

163   make a uniform smear within a 1 cm diameter ring on an agarose-coated microscope

164   slide. This was allowed to air-dry, and then 6 µl of d-H$_2$O plus 3 µl of the nucleic acid

165   dye Syto13 (Invitrogen) was added, and the cells were counted by epifluorescence

166   microscopy using the 100x objective on an Olympus BX60 microscope. Further details

167   on these procedures can be found in (Emerson and Moyer, 2002).

168

169   *2.4 Morphological analysis.* To assess the different morphotypes of iron oxides present in

170   the cassettes, the cell counting samples were subjected to an additional 1:10 dilution and

171   prepared on the counting slides, as described above. Additional dilution ensured minimal

172   overlapping of individual oxide particles on the microscope slide. Images of 8 random

173   microscope fields (40x objective, brightfield) were collected for three different aliquots

174   of the same sample. Imaging was done using a Qicam Fast CCD camera (QImaging,

175   Surrey, BC, Canada) mounted on an Olympus BX60 microscope. The image analysis

176   program ImageJ (https://imagej.nih.gov/nih-image/) was used to quantify the different

177   morphotypes in each image. Morphotypes were classified as sheaths, stalks, Y-shaped

178   structures, filaments, and amorphous oxide particles of no determinate shape. Details on

179   the image analysis and definition of morphotypes has been published elsewhere (Scott et

180   al., 2015). Analysis of colonization slides was done by light microscopy. To qualitatively

181   assess coverage and the different morphotypes present on the slides, arbitrary images

182   (40x objective) were taken at 0.5 cm intervals for the entire length of the 7.5 cm

183   microscope slide.

184   To make representational images of different individual morphotypes of either

185   stalks, Y's, or stick-like filaments, incubation slides were stained with Syto13 and

186   examples of different morphotypes were imaged, either as individual photomicrographs,

187   or several overlapping images were used to make a photomosaic in ImageJ. These images

188   were used to determine the length of individual filaments, either stalks or Y's as reported

189   below, as well as create composite fluorescent and light images to show the juxtaposition

190   of cells producing Fe-oxide structures.

191

192   *2.5 Total iron.* The total amount of Fe-oxides that had accumulated in each cassette, or

193   set of 2 cassettes was determined by diluting a sample of the oxides 1:10 in 0.1 M

194   hydroxylamine to reduce the oxides to Fe(II). This solution was then diluted 1:10 or 1:20

195   into a ferrozine solution to colorimetrically quantify the amount of iron present. Iron was

196   assayed using the ferrozine method (Stookey, 1970) (34) adapted for reading on a

197   Mikroscan 96 well plate reader (Mcbeth et al., 2011).

198

199   *2.6 Fluorescent in situ Hybridization (FISH).* Phylogenetic staining was used to identify

200   the phylogeny of cells attached to Y-shaped iron-oxides. Samples enriched in this

201   morphotype were collected, preserved with paraformaldhyde, washed with PBS, and

202   resuspended in 1:1 PBS ethanol at -20 ˚C until further analysis. Cells attached to the

203   terminal end of Y shaped iron oxides was performed using Catalyzed Activated Reporter

204   Deposition FISH (CARD-FISH; (Pernthaler et al., 2002)) and modified to limit the non-

205   specific binding of probes that occurs in iron-oxide rich samples with several blocking

206   agents (Fleming et al., 2013). Finally, a Cy-3 Zeta proteobacteria specific probe, unlabeled

207   helper probes, and a 20% formamide concentration (Fleming et al., 2013) were used to

208   confirm the phylogenetic affiliation of the Y attached cells.

209

210   *2.7 Community analysis.* We selected 6 samples for 454-pyrosequencing analyses, two

211   from NHR–148h (chambers 1 & 7), two from NHR–256h (chambers 2 & 6), and two

212   from Pohaku (chambers 5 & 8). Samples were processed following previously published

213   protocols (Scott *et al.*, 2015). From each mat sample, approximately 250 mg (wet weight)

214   of mat material was used for DNA extraction from each sample using a Mo Bio

215   PowerSoil® DNA Extraction Kit (Mo Bio Laboratories, Carlsbad CA, USA), modified to

216   include an initial phenol:chloroform:isoamyl alcohol (PCI) step. We found that adding an

217   initial PCI treatment increased final DNA yield from an average < 5ng/µL to

218   concentrations typically > 15 ng/µL (data not shown). Briefly, 200 µL of bead solution

219   was removed from each bead tube and replaced with 200 µL of 25:24:1 PCI (Sigma-

220   Aldrich, St. Louis MO, USA). Samples were then extracted using the manufacture

221   recommended protocol and sent to Research and Testing Laboratory (Lubbock TX, USA)

222   for pyrosequencing. We targeted the V4–V5 hypervariable region of the small subunit

223   rRNA gene (SSU rRNA; *E. coli* positions 531–997) using 530F (5'-GTG CCA GC**M**

224   GC**N** GCG G-3') and 1100R (5'-GGG TT**N** CG**N** TCG TTG-3') following established

225   protocols (Dowd et al., 2008).

226   Sequence processing was performed using mothur v.1.35.0 (Schloss et al., 2009)

227   following previously published methodology (Schloss et al., 2011). Specifically, we used

228   mothur to remove primer and barcode sequences from all reads, as well as any short reads

229   (< 250 bp), reads containing more than six homopolymers, reads with any ambiguities,

230   and/or any chimeric reads detected by UCHIME (Edgar et al., 2011). All quality filtered

231   reads were aligned against a mothur-compatible re-creation

232   (mothur.org/wiki/Silva_reference_files; last accessed 09.11.2016) of the SILVA-SEED

233   (SILVA v123) reference alignment (Quast et al., 2012). Pyrotag reads were classified

234   against the Greengenes reference taxonomy (McDonald et al., 2012). All pyrosequencing

235   libraries are deposited at the European Nucleotide Archive under the sample accessions

236   numbers ERS1466444–ERS1466449, study accession number PRJEB18515. For

237   comparative purposes we included data from iron mats at the Mid-Atlantic Ridge and

238   Lō'ihi (Scott et al., 2016).

239

240   *2.8 Community analysis.*

241   Minimum Entropy Decomposition (MED) (Eren et al., 2014) analysis was performed on

242   the complete dataset of 142,025 reads from 52 samples using the following screening

243   parameters: minimum substantive abundance, 28; minimum entropy value for

244   decomposition, 0.0965; maximum number of discriminants to use for decomposition, 4;

245   maximum variation allowed in each node, 3 nucleotides. Per node normalization was

246   conducted before decomposition based on the node size of the most abundant sequence in

247   the dataset (Eren et al., 2014). Screening removed 18,290 outliers resulting in 123,735

248   total reads in the final analysis. Alignments contained 570 characters with an average

249   read length of 268 base pairs without gaps. Bray-Curtis dissimilarity coefficient (Bray

250   and Curtis, 1957) was used to calculate distance metrics for non-metric multidimensional

251   scaling (NMDS) analyses.

252   In addition, all reads from MED nodes classified as Zetaproteobacteria were

253   classified further using ZetaHunter (https://github.com/mooreryan/ZetaHunter, last

254   accessed 12.05.2016)—a command line script designed to assign SSU rRNA gene

255   sequences to Zetaproteobacteria OTUs (97% identity) (Edgar et al., 2011; Schloss et al.,

256   2009) defined by a reference database with an underlying phylogenetic structure (SILVA

257   v123) (Quast et al., 2012; Pruesse et al., 2012). In the absence of a well-defined

258   taxonomy, OTU binning is currently the accepted method for classifying diversity of

259   Zetaproteobacteria (McAllister et al., 2011), henceforth referred to as ZetaOtus.

260

261   **3. Results and Discussion.**

262   *3.1 Chamber colonization.* The basic design premise for the productivity chambers was

263   that Fe(II)-rich fluids would pass into, and through the fine mesh that enclosed both ends

264   of the cassettes. A portion of the Fe(II) is oxidized inside the cassette resulting in

265   precipitation of Fe-oxides that are large enough (> 100 µm) to be retained by the mesh,

266   thus providing an estimate of accumulation rates for these oxides. A slightly larger mesh

267   opening (100 µm) was used on the cassette exit than on the entrance (50 µm), to reduce

268   the likelihood of back-pressure that could impede flow through the cassette. All the

269   chambers accumulated Fe-oxides; however placement of the chambers on the

270   topologically uneven seafloor, and in the diffuse flow venting proved challenging. At

271   NHR (Mkr 39), four chambers were deployed around the same vent site (Supplemental

272   Fig. 1); two were collected after 148h (6d) and the remaining two were collected at 256h

273   (10.5d). At some point between deployment and 148h, one chamber (#6) fell away from

274   the vent where it was placed, and was redeployed at 148h. Because we do not know the

275   time it was out of the vent flow, this chamber was not used for rate measurements (see

276   below). The four chambers placed at Pokahu (Mkr 57) were inspected after 7d on the

277   seafloor, and there was no visual evidence of Fe-oxides having formed in the cassettes.

278   Therefore, the chambers were re-deployed to another area of flow about 2 m away, and

279   collected after 112h (4.5d). During the intervening period, visible iron oxidation had

280   occurred in all the cassettes associated with these four chambers. The temperature at the

281   vent associated with the Pohaku samplers was constant at around 22°C during the

282   deployment period (Supplemental Fig. 2). At NHR, the temperature was constant for 4 d

283   at 36.5 °C, but then decreased to 25°C and showed some fluctuation between 23.5 and

284   24° until recovery at 6 d (144h), indicating the MTR may have become partially

285   dislodged from the vent (Supplemental Fig. 2). The Fe(II) and O_2 concentrations in the

286   chambers themselves were not measured. The Fe(II) concentrations at NHR vents are

287   between 350 and 450 µM, while at Pohaku the Fe(II) concentrations range from around

288   400 to >600 µM (Glazer and Rouxel, 2009; Scott et al., 2016). These values were

289   measured directly in vent orifices. Due to mixing with seawater there is a rapid drop in

290   Fe(II) concentration away from the vent orifice, thus it would be expected that Fe(II)

291   concentrations in the cassettes could be 5 – 10-fold less than orifice concentrations.

292   Because the summit of Lō'ihi is in an oxygen minima zone, the ambient O_2

293   concentrations are substantially less than fully oxygenated seawater. In 2013, the O_2

294   concentration around NHR was 35 – 38 µM, while at Pohaku it was around 58 µM (Scott

295   et al., 2016).

296

297   We currently recognize three morphotypes of biogenic Fe-oxides that are associated with

298   specific groups of FeOB (Chan et al., 2016). These are helical stalks of the type formed

299   by *Mariprofundus ferrooxydans*, long, round, tubular sheaths produced by filamentous

300   cells belonging to an as yet uncharacterized Zetaproteobacteria, and flattened tubular

301   structures that branch in a characteristic Y-shape, and are referred to here as Y's. The

302   sampling process often breaks these different filamentous oxides into smaller pieces.

303   This, combined with continued mineralization through auto-oxidation of Fe(II) (e.g.

304   (Rentz et al., 2007)), can make it difficult to distinguish individual filaments as a stalk, Y,

305   or sheath, therefore a general filamentous oxide category is also included. Particulate

306   oxides with no definitive morphology can also be common; however, because these

307   resemble abiotically formed oxides, by themselves, they cannot be used as a proxy for

308   biogenic Fe-oxide production. The percentages of the different morphotypes found in the

309   productivity cassettes are shown in Fig. 2. This analysis revealed that recognizable

310   biogenic morphotypes: stalks, Y's, or filaments accounted for the majority (50 – 70%) of

311   oxides at NHR. The exception was chamber 6 in which biogenic and particulate oxides

312   were nearly equal. As noted above, this chamber was temporarily out of the vent flow,

313   which may have led to less biological oxidation (it also had the least abundance of

314   Zetaproteobacteria, see below). By contrast, the Pohaku chambers were dominated by

315   particulate Fe-oxides, and undefined filamentous oxides accounted for most of the

316   remainder.

317

318   *3.2 Iron oxidation rates.* Collecting the iron oxides that accumulated in each cassette

319   revealed the short term incubations at NHR had the greatest accumulation of total iron, an

320   average of 6.2×10^{-3} mol Fe, compared to an average of 3.1×10^{-3} mol for the long term

321   incubation. The shorter term (114h) Pohaku samplers accumulated an average of 1.7 x

322   10^{-3} mol Fe, Table 1. From these values an iron oxidation rate expressed in $mol \cdot hr^{-1}$ was

323   calculated:

324   Fe-ox rate = Total Fe Chamber (moles)/Deployment time (hr)

325 The results for each chamber are shown in Table 1; the rates ranged from a lower value

326 of 8.2 x 10^{-6} mol $\cdot$ hr^{-1} (Pohaku) up to 51.9 x 10^{-6} mol $\cdot$ hr^{-1} (NHR/148hr). The Fe-

327 oxidation rates measured at NHR were 3-fold faster for the 148h deployment than for the

328 256h deployment: 42.1 x 10^{-6} mol $\cdot$ hr^{-1} vs. 12.9 x 10^{-6} mol$\cdot$ hr^{-1}, and the average Pohaku

329 rate, 15.1 x 10^{-6} mol $\cdot$ hr^{-1} was similar to the single longer term NHR deployment

330 (chamber #2).

331 The total number of cells associated with the Fe-oxides in the cassettes ranged

332 from 5 x 10^7 to 4.3 x 10^8, Table 1. Because the 148h incubation at NHR was dominated

333 by recognizable biogenic oxides, and had the most rapid accumulation of oxides, it serves

334 as the best proxy for estimating an Fe-oxidation rate on a per cell basis. The total amount

335 of iron accumulated in these cassettes divided by the total cell number yields an average

336 value of 1.3 x 10^{-16} mol $\cdot$ cell^{-1} $\cdot$ hr^{-1} (SD = .26 x 10^{-16} mol $\cdot$ cell^{-1} $\cdot$ hr^{-1}). This assumes that

337 all the cells counted were FeOB, which is almost certainly not the case. Our amplicon

338 analysis (see below) suggested the relative abundance of Zetaproteobacteria in these

339 chambers was around 80%. If we assume this is a reasonable estimate, and that all the

340 Zetaproteobacteria were oxidizing Fe(II) this gives a value of 1.6 x 10^{-16} mol $\cdot$ cell^{-1} $\cdot$ hr^{-1}.

341 An earlier analysis of Fe-oxidation by a pure culture of *M. ferrooxydans* estimated that

342 cell growth required 9.16 x 10^{-15} mol Fe(II) per cell (Chan et al., 2010). This assumed a

343 12h doubling time for *M. ferroxydans*, and at this rate this would equate to an Fe-

344 oxidation rate of 7.7 x 10^{-16} mol $\cdot$ cell^{-1} $\cdot$ hr^{-1}. An estimate for the rate of Fe-oxidation for

345 *M. ferrooxydans* grown on a cathode, where uptake of electrons was used as a proxy for

346 Fe-oxidation gave a significantly higher rate of 7.5 x 10^{-14} mol $\cdot$ cell^{-1} $\cdot$ hr^{-1} (Summers et

347 al., 2012). The *in-situ* cell-based Fe-oxidation rates from the cassettes is also less than

348   estimates of Fe-oxidation rates for pure cultures of freshwater FeOB that range from 0.8

349   – 14 x 10^{-14} mol · $cell^{-1}$ · hr^{-1} (Chan et al, 2016). It is not surprising the *in situ* rates

350   reported here are less than laboratory rates, since the latter represent the more ideal

351   conditions of controlled growth. Because the *in situ* growth chambers are designed as

352   flow through devices, presumably there was a net loss of cells and Fe-oxides from the

353   cassettes during the incubation period that would result in a reduced rate of oxidation. On

354   the other hand, a lower per cell rate of Fe-oxidation could also suggest FeOB in these

355   natural populations may be more efficient at oxidizing Fe(II) than the isolates.

356

357   *3.3 Surface Colonization.* All the colonization slides placed within the chambers at both

358   NHR and Pohaku showed evidence for formation of biogenic oxides (results not shown).

359   The most common biogenic morphotypes were Y's and helical stalks. Sheath

360   morphotypes were rare; nor were sheaths observed in the cassettes, indicating sheath-

361   forming Zetaproteobacteria did not colonize the chambers. At Loihi, sheath-forming

362   Zetaproteobacteria are responsible for forming mats with a veil-like appearance. These

363   veil-like mats form farther from vent fluid sources (e.g. in cooler regions with more O_2

364   and less Fe(II) compared to mats where stalks and Y's predominate (Scott et al., 2016).

365   The cells that produce the Y-structures are easily detached during sampling (Chan

366   et al., 2016), and the freshly produced Y-type structures that were plentiful in the

367   cassettes had few apical cells associated with them. However, on the colonization slides

368   the apical cells responsible for tube formation were relatively common, Fig. 3.

369   Presumably direct attachment of the structures to the slides resulted in less disturbance

370   and loss of cells upon sample recovery. The total length of individual Y structures on

371   colonization slides ranged from 5.2 – 49.5 μm with a median length of 11.2 μm (SD =

372   2.6), Table 2. We estimated the rate of Y-filament formation by selecting the longest

373   filaments that were observed on a given set of slides and dividing by the deployment

374   time. The most rapid production rate for Y's was 0.34 μm · hr^{-1} (Pohaku), while the

375   average was 0.19 μm · hr^{-1} (SD = 0.11 μm · hr^{-1}). To demonstrate that these presumptive

376   Fe-oxidizers were members of the Zetaproteobacteria, a sample from NHR with a good

377   representation of cells coupled to filaments was stained with a FISH probe specific for

378   the Zetaproteobacteria. This resulted in staining of the terminal cells, thus confirming

379   these cells are Zetaproteobacteria, Fig. 4.

380   Stalks, similar to those produced by *M. ferrooxydans*, were also observed on the

381   colonization slides, Supplemental Fig. 3, and single stalks that had at least one cell

382   division were common. The longest stalks could be 100's of μm in length, with a range

383   measured between 25 – 390 μm for individual stalks. Using the same criteria as described

384   for the Y's above, stalk production rates were estimated to range from 0.7 – 2.1 μm · hr^{-1},

385   with an average of 1.32 μm · hr^{-1} (SD = 0.62 μm · hr^{-1}), table 2.

386   A novel cell/oxide morphotype, with a stick-like appearance, was also

387   documented on the colonization slides. This was a very thin rod <0.5 μm in diameter

388   coated in iron oxyhydroxides, see Fig. 5. These stick-like iron oxide structures are

389   commonly observed in marine iron mats (D. Emerson, unpublished observations), and in

390   our morphological analysis are grouped with filamentous oxides of unknown provenance.

391   So far as we are aware, this is the first time that cells have been observed associated with

392   these structures in a way that indicates their genesis, and suggests this could be a novel

393   group of FeOB. Alternatively, they could be cells that are simply being encased in Fe-

394   oxyhydroxides as a result of abiotic Fe-oxidation. The majority of the stick-like structures

395   did not have cells present; however this is consistent with other biogenic oxides where

396   the majority of the structures are uninhabited (Chan et al., 2016). We were unable to

397   visualize any of these cells using FISH, so we do not know if they belong to the

398   Zetaproteobacteria.

399

400   *3.4 Community Analysis.* Amplicon-based analysis of the SSU rRNA gene was used to

401   assess the relative abundances of different bacterial populations within the chambers, as

402   well as assess overall diversity between sites, temporally and spatially, and contrast

403   populations in freshly formed iron mats to bulk iron mat communities. All the chamber

404   samples were dominated by Zetaproteobacteria. The shorter term deployments had

405   relative abundances of Zetaproteobacteria that were between 81 and 87% of the total

406   sequences, while in the two 256h deployments at NHR, the relative abundances were 74

407   and 31%, Table 3. The communities from three of the chambers (1,2, and 7) from NHR

408   clustered closely together, and grouped with a large cluster of samples from both NHR

409   and S. Hiolo Ridge, while chamber 6 did not cluster with the other NHR samples,

410   (Supplemental Fig. 4). We speculate that the period chamber 6 was not in vent flow may

411   have resulted in colonization of the iron oxides in the cassettes by other, non-FeOB. The

412   microbial communities in the two chambers (5 & 8) at Pohaku clustered with a group of

413   six community iron mat samples, five of which were from Pohaku, indicating that the

414   organisms colonizing the chambers were most closely related to those found in the iron

415   mats at this site (Supplemental Fig. 4). Despite having relatively low abundances of

416   recognizably biogenic oxides, the Pohaku chambers still had high percentages of

417 Zetaproteobacteria, indicating that not all Fe-oxidizing Zetaproteobacteria produce

418 recognizable filamentous morphotypes.

419   A more detailed OTU analysis of the Zetaproteobacteria, (Fig. 6), revealed that all

420 the NHR samples had the same representation of Zeta OTUs, although the relative

421 abundances varied. By contrast, in the two Pohaku samples ZetaOtu 1 and ZetaOtu 2

422 together accounted for over 90% of the Zetaproteobacteria reads. When the populations

423 in the chambers as a whole were compared to microbial mat samples either from Lō'ihi

424 or the Mid-Atlantic Ridge (MAR) (Fig. 6), ZetaOtu 9 was notable for its absence in the

425 chambers. Notable for its presence in the chambers, but absence in mature mats, was

426 ZetaOtu 11. In general, ZetaOtu 11 is rarely found in marine iron mats (McAllister et al.,

427 2011; Scott et al., 2016), despite there being several stalk-forming isolates from this

428 group, including *Mariprofundus ferrooxydans*. The chamber results suggest ZetaOtu 11

429 may be a signature early colonizer of iron mats, and due to its stalk-forming abilities

430 could play an important role in the genesis of stable mat communities (Chan et al., 2016).

431   Overall, this community analysis compares and contrasts in interesting ways from

432 an earlier colonization study at Lō'ihi done by Rassa, et al (Rassa et al., 2009). That study

433 evaluated a more diverse group of vent sites at Lō'ihi, both short-term (4 – 10d) and

434 long-term (e.g. 1 year). A different type of colonization chamber that was packed tightly

435 with glass wool was used, and the morphotypes of the FeOB present was not evaluated.

436 Clone libraries (SSU rRNA gene) of short-term incubations were dominated by clones of

437 Zetaproteobacteria from cooler vents (22°C), very similar to what we observed in this

438 study. At the time of the Rassa, et al study, there were also higher temperature vent (64 –

439 77°C) sites at Lō'ihi, and these had higher abundances of putative sulfur-metabolizing

440   Epsilonproteobacteria (Rassa et al., 2009). Epsilonproteobacteria were only a minor

441   member of the communities we analyzed from these intermediate temperature (40 – 50°)

442   vents that are the hottest fluids currently observed at Lō'ihi. This suggests that as the

443   vents have cooled Zetaproteobacteria have become more prevalent, and is consistent with

444   detectable sulfide being largely absent from the vent fluids in 2013 (Scott et al., 2016.).

445   Terminal restriction fragment length polymorphisms (T_RFLPs) were used in the earlier

446   study to analyze community composition, and an increase in the complexity of the

447   community was noted in long term, versus short term colonization experiments (Rassa et

448   al., 2009). The same trend was noted in this study using amplicon analysis that provides

449   greater resolution of community diversity than T_RFLP; however since only short term

450   deployments were done for this study, it is not possible to make direct comparisons.

451

452   *3.5 Mat accretion.* It is important to understand the accretion rates of these iron mats,

453   both for overall microbial mat development, and to determine the potential for biogenic

454   iron mats to serve as an iron source to the surrounding ocean. Recent work from Lō'ihi

455   has shown the primary structural element of the mats are filamentous stalks, or sheaths

456   (Chan et al., 2016). The stalks observed on colonization slides then can serve as a proxy

457   for estimating mat accretion rates of stalk-dominated mats.   The most rapid rate of stalk

458   formation observed on a colonization slide was estimated at 2.6 µm/h. This rate is based

459   on the assumption that the cells attached shortly after the slide was deployed and were

460   continuously present until the chamber was retrieved. A stalk production rate of 2.2 µm/h

461   was reported for a pure culture of *M. ferrooxydans* (Chan et al., 2010) based on time-

462   lapse imaging, thus the *in situ* estimate is in the same range as the *in vitro* rate. Based on

463 this analysis, if we assume a stalk production rate of 2.5 µm/h, cells that colonize a

464 surface and grow uniformly should accrete at a rate of 60 µm/d, or approximately 420

465 µm/week. This works out to around 2.2 cm/yr. This is a necessarily simplistic

466 extrapolation of a complex process, i.e. in an actual mat there are multiple colonization

467 events, and it's unlikely the cells exhibit long-term, uniform growth rates. Nonetheless, it

468 provides an approximation of how fast entire, vent-associated iron mat structures may

469 grow. Interestingly, these estimates for the growth of marine iron mats are substantially

470 slower than the accretion rates of up to 2.2 mm $\cdot$ d^{-1} measured in a freshwater microbial

471 iron mat (Emerson and Revsbech, 1994). The stalk-forming freshwater FeOB *Gallionella*

472 *ferruginea* can produce stalk at rates up to 80 µm/h, or nearly 40 times faster than *M.*

473 *ferrooxydans* (Hanert, 1973). Thus, it is reasonable to assume that freshwater iron mats

474 can accrete much more rapidly than marine iron mats.

475   To further determine if our estimate for the growth rates of marine iron mats is

476 realistic, we did an intentional mat removal experiment at Lō'ihi, by suctioning away a

477 beehive shaped mat that was approximately 30 cm tall and fed by a single diffuse flow

478 orifice on the ocean floor (Supplemental Fig 4). The site was monitored twice more

479 during our expedition, with the last visit coming 10d after removal. While there appeared

480 to be subtle changes at this site, there was not an obvious, visible amount of mat accretion

481 over 10d (Supplemental Fig. 5). Based on our calculations above, the mat would only

482 accumulate to a thickness of <1 mm during these short-term observations. This would be

483 less than could be detected visually with the ROV, thus the fact we did not visibly

484 observe accretion in 10 days is consistent with our estimates. This was intended to be a

485 long-term re-colonization experiment, but, as yet, no subsequent observations have been

486   made of this site. At the Pohaku and NHR vent sites when mat was removed during

487   sample collection with the large suction sampler on ROV *Jason*, we did not detect

488   significant regrowth of the iron mats over the course of an expedition, 10 – 12 days. An

489   example is shown in Supplemental Fig. 6. These same sites had been visited and sampled

490   extensively on a prior expedition to Lō'ihi 18 months earlier; however, during the 2013

491   expedition there was no obvious sign of the previous disturbance, indicating these 2 – 5

492   cm thick mats had fully recovered in the intervening time, which would be expected

493   based on our estimates. Thus, our estimates for mat accretion based on observations of

494   rates of stalk-formation seem consistent with visual observations of mat accretion at

495   Lō'ihi.

496

497   **4. Conclusions.**

498   The *in-situ* growth chambers proved capable of capturing the growth of biogenic iron

499   oxides, and revealed a diversity of morphotypes associated with FeOB. This work

500   provides an initial estimate for *in-situ* iron oxidation rates for marine Fe-oxidizing

501   bacteria, as well as an estimate for the rate at which iron mats can accrete around diffuse

502   flow hydrothermal vents on the seafloor. An amplicon-based sequence analysis of newly

503   formed Fe-oxides in the chambers revealed Zetaproteobacteria as the dominant

504   phylotype, with a relative abundance as high as 89%. There was a trend towards

505   decreasing relative abundance of Zetaproteobacteria, and increasing overall diversity with

506   incubation time. Colonization slides revealed abundant evidence for colonization by

507   stalk-forming and Y-producing FeOB, as well as a novel stick-like oxide that appeared to

508   be a direct product of microbial iron oxidation. Analysis of the Y-producing microbes

509   using FISH revealed they are members of the Zetaproteobacteria.

510

511

512   Acknowledgements.

516

517

518   **References.**

519

520   Bennett, S.A., Hansman, R.L., Sessions, A.L., Nakamura, K.-I., Edwards, K.J., 2011.
521   Tracing iron-fueled microbial carbon production within the hydrothermal plume at
522   the Loihi seamount. Geochim. Cosmochim. Acta 75, 5526–5539.
523   doi:10.1016/j.gca.2011.06.039
524   Handley, K.M., Boothman, C., Mills, R.A., Pancoast, R.D., Lloyd, J.R., 2010. Functional
525   diversity of bacteria in a ferruginous hydrothermal sediment. ISME J 4, 1193–1205.
526   doi:10.1038/ismej.2010.38
527   Bray, J.T., Curtis, J.T., 1957. An ordination of upland forest communities of southern
528   Wisconsin. Ecol. Mono. 27, 325–349.
529   Chan, C.S., Fakra, S.C., Emerson, D., Fleming, E.J., Edwards, K.J., 2010. Lithotrophic
530   iron-oxidizing bacteria produce organic stalks to control mineral growth:
531   implications for biosignature formation. ISME J 5, 717–727.
532   doi:10.1038/ismej.2010.173
533   Chan, C.S., McAllister, S.M., Leavitt, A.H., Glazer, B.T., Krepski, S.T., Emerson, D.,
534   2016. The architecture of iron microbial mats reflects the adaptation of
535   chemolithotrophic iron oxidation in freshwater and marine environments. Front.
536   Microbiol. 7, 447. doi:10.3389/fmicb.2016.00796
537   Dowd, S.E., Callaway, T.R., Wolcott, R.D., Sun, Y., McKeehan, T., Hagevoort, R.G.,
538   Edrington, T.S., 2008. Evaluation of the bacterial diversity in the feces of cattle using
539   16S rDNA bacterial tag-encoded FLX amplicon pyrosequencing (bTEFAP). BMC
540   Microbiol. 8, 125. doi:10.1186/1471-2180-8-125
541   Edgar, R.C., Haas, B.J., Clemente, J.C., Quince, C., Knight, R., 2011. UCHIME
542   improves sensitivity and speed of chimera detection. Bioinformatics. 27, 2194–2200.
543   doi:10.1093/bioinformatics/btr381
544   Emerson, D., 2016. The Irony of Iron – Biogenic iron oxides as an iron source to the
545   ocean. Front. Microbiol. 6, 84. doi:10.1038/ngeo1148
546   Emerson, D., Moyer, C.L., 2002. Neutrophilic Fe-oxidizing bacteria are abundant at the
547   Loihi Seamount hydrothermal vents and play a major role in Fe oxide deposition.
548   Appl. Environ. Microbiol. 68, 3085–3093. doi:10.1128/AEM.68.6.3085-3093.2002
549   Emerson, D., Revsbech, 1994. Investigation of an iron-oxidizing microbial mat
550   community located near Aarhus, Denmark: field studies. Appl. Environ. Microbiol.
551   60, 4022-4031.
552   Eren, A.M., Morrison, H.G., Lescault, P.J., Reveillard, J., Vineis, J.H., Sogin, M.L., 2014.
553   Minimum entropy decomposition: Unsupervised oligotyping for sensitive
554   partitioning of high-throughput marker gene sequences. ISME J. 9: 968-979
555   Fleming, E.J., Davis, R.E., McAllister, S.M., Chan, C.S., Moyer, C.L., Tebo, B.M.,
556   Emerson, D., 2013. Hidden in plain sight: discovery of sheath-forming, iron-
557   oxidizing Zetaproteobacteria at Loihi Seamount, Hawaii, USA. FEMS Microbiol.
558   Ecol. 85, 116–127. doi:10.1111/1574-6941.12104
559   German, C.R., Legendre, L.L., Sander, S.G., Niquil, N., Luther, G.W., III, Bharati, L.,
560   Han, X., Le Bris, N., 2015. Hydrothermal Fe cycling and deep ocean organic carbon
561   scavenging: Model-based evidence for significant POC supply to seafloor sediments.
562   Earth Planetary Sci. Lett. 419, 143–153. doi:10.1016/j.epsl.2015.03.012
563   Glazer, B.T., Rouxel, O.J., 2009. Redox speciation and distribution within diverse iron-

564   dominated microbial habitats at Loihi Seamount. Geomicrobiol. J. 26, 606–622.
565   doi:10.1080/01490450903263392
566 Hanert, H., 1973. Quanifizierung der massenentwicklung des eisenbakteriums Gallionella
567   ferruginea unter naturlichen bedingungen. Arch Microbiol 88, 225–243.
568 Johnson, C.M., Beard, B.L., Roden, E.E., 2008. The iron isotope fingerprints of redox
569   and biogeochemical cycling in modern and ancient Earth. Annu. Rev. Earth Planet.
570   Sci 36, 457–493. doi:10.1146/annurev.earth.36.031207.124139
571 Kato, S., Ishibashi, J.-I., Kimura, H., Yamagishi, A., 2009. Abundance of
572   Zetaproteobacteria within crustal fluids in back-arc hydrothermal fields of the
573   Southern Mariana Trough. Environ. Microbiol. 11, 3210–3222. doi:10.1111/j.1462-
574   2920.2009.02031.x
575 Kennedy, C., Scott, S., Ferris, F., 2004. Hydrothermal phase stabilization of 2-line
576   ferrihydrite by bacteria. Chem. Geol. 212, 269–277.
577   doi:10.1016/j.chemgeo.2004.08.017
578 McAllister, S.M., Davis, R.E., Mcbeth, J.M., Tebo, B.M., Emerson, D., Moyer, C.L.,
579   2011. Biodiversity and emerging biogeography of the neutrophilic iron-oxidizing
580   Zetaproteobacteria. Appl. Environ. Microbiol. 77, 5445–5457.
581   doi:10.1128/AEM.00533-11
582 Mcbeth, J.M., Little, B.J., Ray, R.I., Farrar, K.M., Emerson, D., 2011. Neutrophilic iron-
583   oxidizing "zetaproteobacteria" and mild steel corrosion in nearshore marine
584   environments. Appl. Environ. Microbiol. 77, 1405–1412. doi:10.1128/AEM.02095-
585   10
586 Melton, E.D., Swanner, E.D., Behrens, S., Schmidt, C., Kappler, A., 2014. The interplay
587   of microbially mediated and abiotic reactions in the biogeochemical Fe cycle. Nat.
588   Rev. Micro. 12, 797–809. doi:10.1038/nrmicro3347
589 Pernthaler, A., Pernthaler, J., Amann, R., 2002. Fluorescence in situ hybridization and
590   catalyzed reporter deposition for the identification of marine bacteria. Appl. Environ.
591   Microbiol. 68, 3094-3101.
592 Picard, A., Kappler, A., Schmid, G., Quaroni, L., Obst, M., 2015. Experimental
593   diagenesis of organo-mineral structures formed by microaerophilic Fe(II)-oxidizing
594   bacteria. Nat. Comm. 6, 1–8. doi:10.1038/ncomms7277
595 Pruesse, E., Peplies, J., Glockner, F.O., 2012. SINA: Accurate high-throughput multiple
596   sequence alignment of ribosomal RNA genes. Bioinformatics 28, 1823–1829.
597   doi:10.1093/bioinformatics/bts252
598 Quast, C., Pruesse, E., Yilmaz, P., Gerken, J., Schweer, T., Yarza, P., et al. 2012. The
599   SILVA ribosomal RNA gene database project: improved data processing and web-
600   based tools. Nucleic Acids Res. 41: D590–D596.
601 Rassa, A.C., McAllister, S.M., Safran, S.A., Moyer, C.L., 2009. Zeta-Proteobacteria
602   dominate the colonization and formation of microbial mats in low-temperature
603   hydrothermal vents at Loihi Seamount, Hawaii. Geomicrobiol. J. 26, 623–638.
604   doi:10.1080/01490450903263350
605 Rentz, J.A., Kraiya, C., Luther, G.W., Emerson, D., 2007. Control of ferrous iron
606   oxidation within circumneutral microbial iron mats by cellular activity and
607   autocatalysis. Environ. Sci. Technol. 41, 6084–6089.
608 Resing, J.A., Sedwick, P.N., German, C.R., Jenkins, W.J., Moffett, J.W., Sohst, B.M.,
609   Tagliabue, A., 2015. Basin-scale transport of hydrothermal dissolved metals across

610   the South Pacific Ocean. Nature 523, 200–203. doi:10.1038/nature14577

611 Schloss, P.D., Gevers, D., Westcott, S.L., 2011. Reducing the Effects of PCR
612   Amplification and Sequencing Artifacts on 16S rRNA-Based Studies. PLoS ONE 6,
613   e27310. doi:10.1371/journal.pone.0027310.t004

614 Schloss, P.D., Westcott, S.L., Ryabin, T., Hall, J.R., Hartmann, M., Hollister, E.B.,
615   Lesniewski, R.A., Oakley, B.B., Parks, D.H., Robinson, C.J., Sahl, J.W., Stres, B.,
616   Thallinger, G.G., Van Horn, D.J., Weber, C.F., 2009. Introducing mothur: Open-
617   Source, Platform-Independent, Community-Supported Software for Describing and
618   Comparing Microbial Communities. Appl. Environ. Microbiol. 75, 7537–7541.
619   doi:10.1128/AEM.01541-09

620 Scott, J.J., Breier, J.A., Luther, G.W., Emerson, D., 2015. Microbial iron mats at the Mid-
621   Atlantic ridge and evidence that Zetaproteobacteria may be restricted to iron-
622   oxidizing marine systems. PLoS ONE 10, e0119284.
623   doi:10.1371/journal.pone.0119284.t002

624 Scott, J.J., Glazer, B.T., Emerson, D., 2016. Bringing microbial diversity into focus:
625   high-resolution analysis of iron mats from the Loihi Seamount. Environ. Microbiol.
626   In Press. doi:10.1111/1462-2920.13607

627 Stookey, L.L., 1970. Ferrozine-a new spectrophotometric reagent for iron. Anal. Chem.
628   42, 779–781.

629 Summers, Z.M., Gralnick, J.A., Bond, D.R., 2012. Cultivation of an obligate Fe(II)-
630   Oxidizing lithoautotrophic bacterium using electrodes. mBio 4, e00420–12–e00420–
631   12. doi:10.1128/mBio.00420-12

632 Toner, B.M., Berquo, T.S., Michel, F.M., Sorensen, J.V., Templeton, A.S., Edwards, K.J.,
633   2012. Mineralogy of iron microbial mats from loihi seamount. Front. Microbiol.
634   3:118. doi:10.3389/fmicb.2012.00118/

635 Toner, B.M., Fakra, S.C., Manganini, S.J., Santelli, C.M., Marcus, M.A., Moffett, J.W.,
636   Rouxel, O., German, C.R., Edwards, K.J., 2009. Preservation of iron(II) by carbon-
637   rich matrices in a hydrothermal plume. Nature Geosci. 2, 197–201.
638   doi:10.1038/ngeo433

639

640

641   Table 1. Fe-oxidation rates at NHR and Pohaku. The values for chambers for NHR were
642   calculated from each individual cassette, while values for Pohaku are from the combined
643   cassettes from each chamber. Chamber 6 from NHR is not included in this analysis.
644

Chamber	Site	Hours	Total Fe (10^{-6} mol)	Total cells	Fe-oxid 10^{-6} mol $\cdot$ hr^{-1}	Fe-oxidized per cell 10^{-16} mol $\cdot$ hr^{-1} $\cdot$ cell^{-1}
ST1a	NHR	148	3882	1.70E+08	26.2	1.54
ST1b	NHR	148	7674	3.59E+08	51.9	1.44
ST7a	NHR	148	6229	4.17E+08	42.1	1.01
ST7b	NHR	148	7125	4.33E+08	48.1	1.11
Average (St Dev)			**6228 (1673)**	**3.5E+08 (1.1E+08)**	**42.1 (11.3)**	**1.3 (.26)**
ST2a	NHR	256	3966	4.14E+08	15.5	0.38
ST2b	NHR	256	2090	7.97E+07	8.2	1.05
Average (St Dev)			**3028 (1326)**	**2.5E+08 (2.4E+08)**	**11.8 (5.2)**	**0.72 (0.4)**
ST3	Pohaku	112	919	5.05E+07	8.2	1.63
ST4	Pohaku	112	2070	8.74E+07	18.5	2.04
ST5	Pohaku	112	2082	7.72E+07	18.6	2.31
ST8	Pohaku	112	1686	1.24E+08	15.1	1.12
Average (St Dev)			**1689 (546)**	**8.5E+07 (3.1E+07)**	**15.1 (4.9)**	**1.8 (0.53)**

645
646

647

648 Table 2. Filamentous iron oxide production rates for stalks and Y's, calculated from
649 measurements made on colonization slides.

650

Stalks

Chamber	Site	Hrs	n	Filament length (μm)	Median length (μm)	SD	Average length top 10%	Rate μm/hr	SD
1	NHR	148	16	76 - 390	148	77	307	2.1	
7	NHR	148	22	25-277	83	46	207	1.4	
6	NHR	256	19	49-162	95	39	177	0.7	
2	NHR	256	20	45-200	89	40	171	0.7	
3	Pohaku	112	18	58-207	115	43	191	1.7	
Average					**106**	**26**		**1.32**	**0.62**

Y's

Chamber	Site	Hrs	n	Filament length (μm)	Median length (μm)	SD	Average length top 10%	Rate μm/hr	SD
1	NHR	148	28	7.3-15.5	11.9	2.5	15	0.1	
2	NHR	256	19	5.2-17.3	7.8	3.4	16	0.06	
7	NHR	148	16	6.5-15.7	9.5	2.4	15	0.1	
5	Pohaku	112	24	9.0-27.0	14	5.4	28.3	0.25	
3	Pohaku	112	27	8.0-49.5	14.2	8.3	38.3	0.34	
8	Pohaku	112	11	9.0-27	9.7	6.4	29	0.26	
Average					**11.2**	**2.6**		**0.185**	**0.11**

651
652
653
654
655
656

657
658
659   Table 3. Relative abundance of Zetaproteobacteria reads compared to total reads from the
660   different chambers based on the SSU 16S rRNA amplicon analysis.
661

Chamber	Site	Time(h)	Zeta-Reads	Total Reads	% Zeta-Reads
1	NHR	148	1006	1209	83.2
7	NHR	148	2800	3237	86.5
2	NHR	256	1541	1979	77.9
6	NHR	256	476	1427	33.4
5	Pohaku	112	2278	2610	87.3
8	Pohaku	112	4473	5048	88.6

662
663
664
665
666
667
668
669
670
671
672
673
674
675

676
677　Figure legends.
678
679　Fig. 1. A diagram of the productivity chambers showing the central body of the chamber
680　with that held the microscope slides, and the two cassettes, covered on both ends with
681　Nitex mesh. The cassettes had screwcaps at both ends that were used to hold the mesh
682　that was cut to fit the openings.
683
684　Fig. 2. Pie charts showing the percentages of different morphotypes of iron oxides from
685　the different cassettes. The oxide morphology was determined by light microscopy as
686　described in the text.
687
688　Fig. 3. A photo-montage from an *in-situ* microscope slide of Y-shaped filaments with
689　cells associated with the ends of the filaments. The left set of panels are overlays of
690　epifluorescence and phase contrast images, cells are stained green at the end of the
691　filaments, denoted by arrows in a, b, and e. The right hand panel are the original phase
692　contrast images, note cells are not visible. The marker bar = 5 μm.
693
694　Fig. 4. FISH-probe for Zetaproteobacteria staining apical cells in Y-shaped structures.
695　Panel a, phase contrast image of the Y-shaped structure, the cells are not visible; b,
696　composite epifluorescence and brightfield image of the particle; c, the epifluorescence
697　image of FISH-probe showing cells alone. The scale bar = 5 μm.
698
699　Fig. 5. A photo-montage from an in-situ microscope slide of stick-like iron oxides with
700　cells. The left panels are overlays of epifluorescence and phase contrast images showing
701　the juxtaposition of cells and oxides. The right hand panels are the original phase contrast
702　images. The marker bar = 5 μm.
703
704　Fig. 6. SSU rRNA amplicon community analysis of Zetaproteobacteria present in
705　chambers and iron mats. The left-hand set of columns show the relative abundance of
706　different ZetaOtus from the different incubation chambers. The right-hand columns
707　compare a sample that integrates all the chamber Zetaproteobacteria reads with either veil
708　or non-veil communities in mature Loihi iron mats, or iron mats from the Mid-Atlantic
709　Ridge (MAR). Note the presence of Otu11 in the chambers, and absence from the mats;
710　not the absence of Otu9 in the chambers, but presence in the mats. The data for the iron
711　mat comparisons are taken from Scott et al 2016.
712
713　Supplemental Figures.
714　Supplemental Fig. 1. An image showing the placement of in-situ incubation chambers
715　(1,2,6, and 7) on diffuse vents associated with NHR.
716
717　Supplemental Fig. 2. Temperature graphs from the MTRs placed at NHR and Pohaku.
718　The arrows denote time of deployment and recovery.
719

720   Supplemental Fig. 3. A photomosaic from an *in situ* microscope slide of filamentous stalk
721   formation. This represents colonization events by several individual stalk-forming cells.
722   The marker bar = 10 μm.
723

724   Supplemental Fig. 4. MED comparison of the total bacterial community composition of
725   the different chambers with 49 iron mat samples collected from different vents at Loihi or
726   from the MAR. The yellow colored panels (top) and arrows (bottom) indicate chambers.
727   The data from other vent sites is taken from Scott *et al* 2016.
728

729   Supplemental Fig. 5. Mat removal experiment, a beehive shaped iron mat, left panel, had
730   a black frame placed around it and the mat was removed using the large suction sampler
731   on the ROV *Jason,* and then monitored for 10d. During this time there was little re-
732   growth of the mat. The white bar in the left hand panel = 10 cm, the black frame is
733   approximately 40 cm on each side.
734

735   Supplemental Fig. 6. Before and after images from mat sampling on NHR. The left hand
736   panel was taken just prior to sampling with the large suction sampler on ROV *Jason* on
737   3/19/13, and the right hand image was taken 11d later. A primary vent orifice can be seen
738   as the gray-colored mineral near the bottom of the left hand image. The white circle
739   denotes the approximate sampling area, note there does not appear to be obvious
740   regrowth of the mat during this time.
741

742   Fig 1.

743

744   Fig. 1. A diagram of the productivity chambers showing the central body of the chamber
745   with that held the microscope slides, and the two cassettes, covered on both ends with
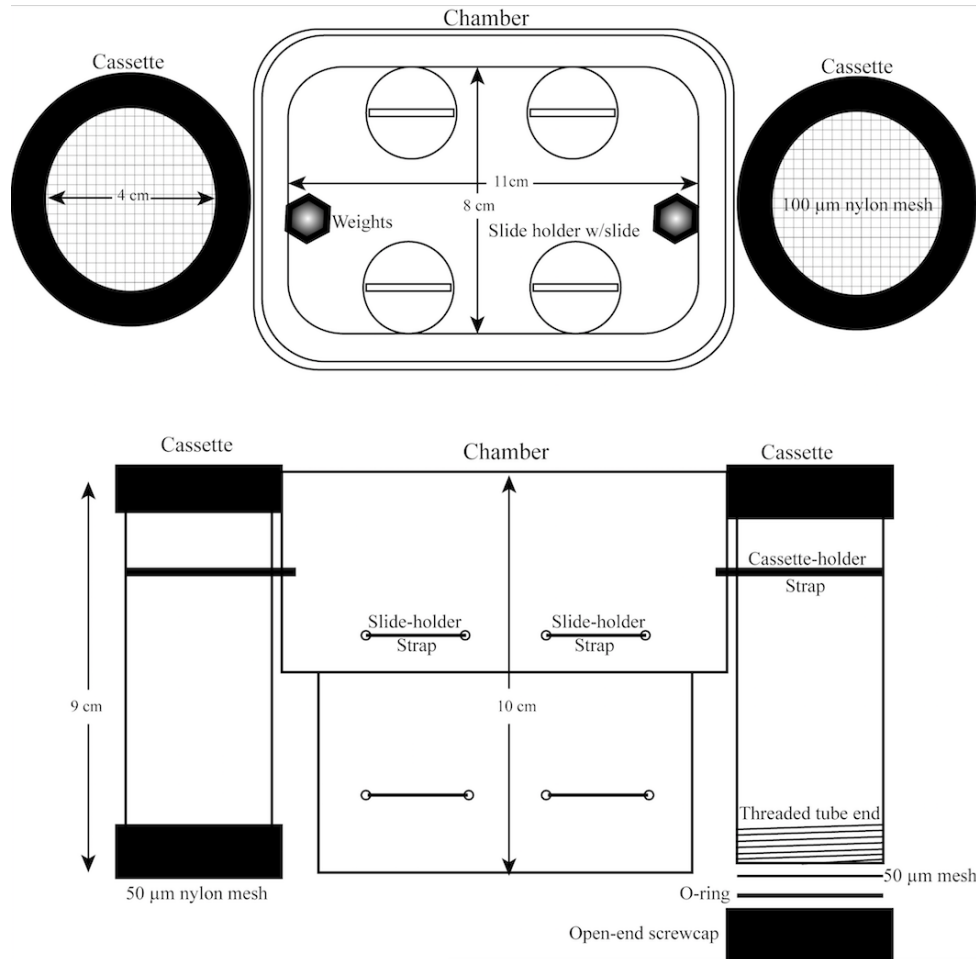746   Nitex mesh. The cassettes had screwcaps at both ends that were used to hold the mesh
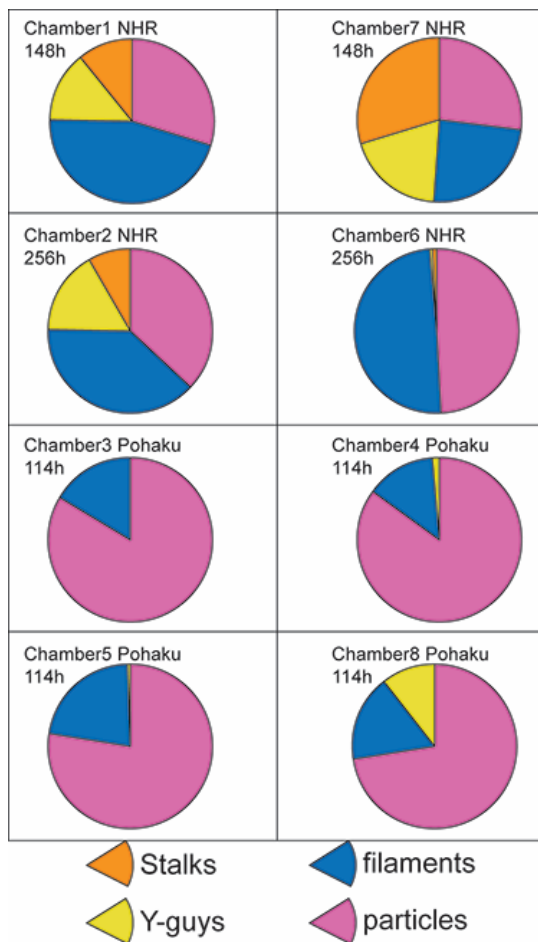747   that was cut to fit the openings.

748

749

750

751

752
753
754

755   Fig. 2
756   Pie charts showing the percentages of different morphotypes of iron oxides from the
757   different cassettes. The oxide morphology was determined by light microscopy as
758   described in the text.
759
760
761
762

763
764
765
766
767

768   Fig. 3

769   A photo-montage from an *in-situ* microscope slide of Y-shaped filaments with cells

770   associated with the ends of the filaments. The left set of panels are overlays of

771   epifluorescence and phase contrast images, cells are stained green at the end of the

772   filaments, denoted by arrows in a, b, and e. The right hand panel are the original phase

773   contrast images, note cells are not visible. The marker bar = 5 μm.

774

775

776

777
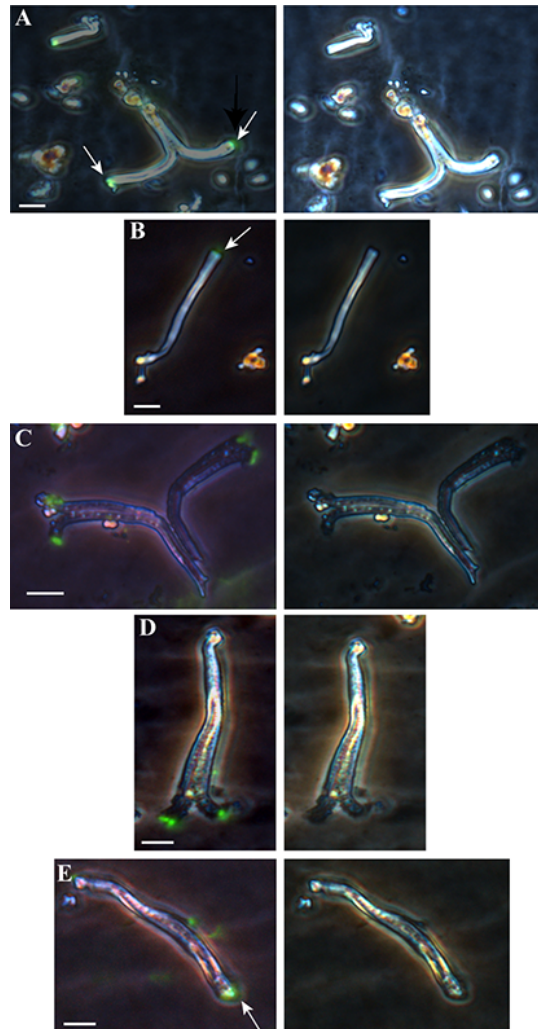
778
779
780
781

782   Fig. 4

783   FISH-probe for Zetaproteobacteria staining apical cells in Y-shaped structures. Panel a,

784   phase contrast image of the Y-shaped structure, the cells are not visible; b, composite

785   epifluorescence and brightfield image of the particle; c, the epifluorescence image of

786   FISH-probe showing cells alone. The scale bar = 5 μm.

787

788

789

790

791
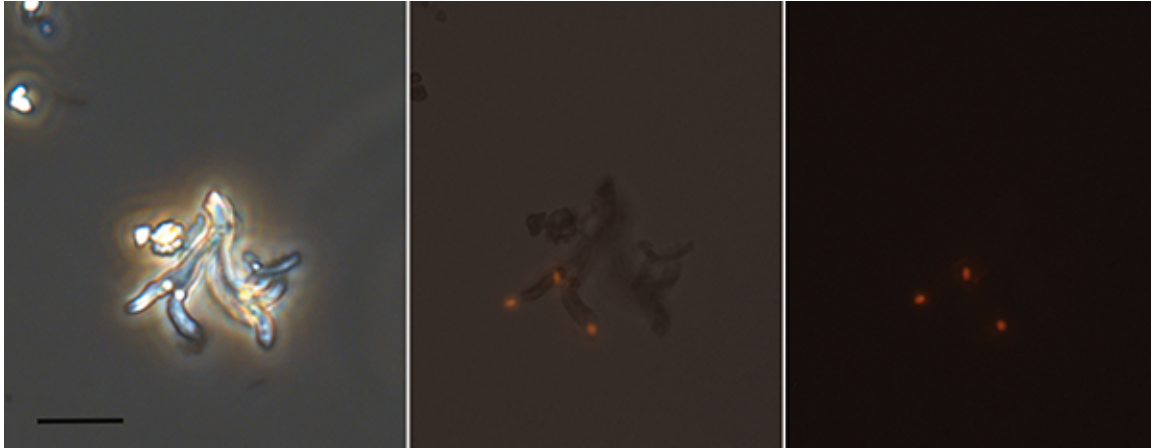
792

793

794

795

796

797

798

799   Fig. 5

800   Fig. 5. A photo-montage from an in-situ microscope slide of stick-like iron oxides with

801   cells. The left panels are overlays of epifluorescence and phase contrast images showing

802   the juxtaposition of cells and oxides. The right hand panels are the original phase contrast

803   images. The marker bar = 5 μm.

804
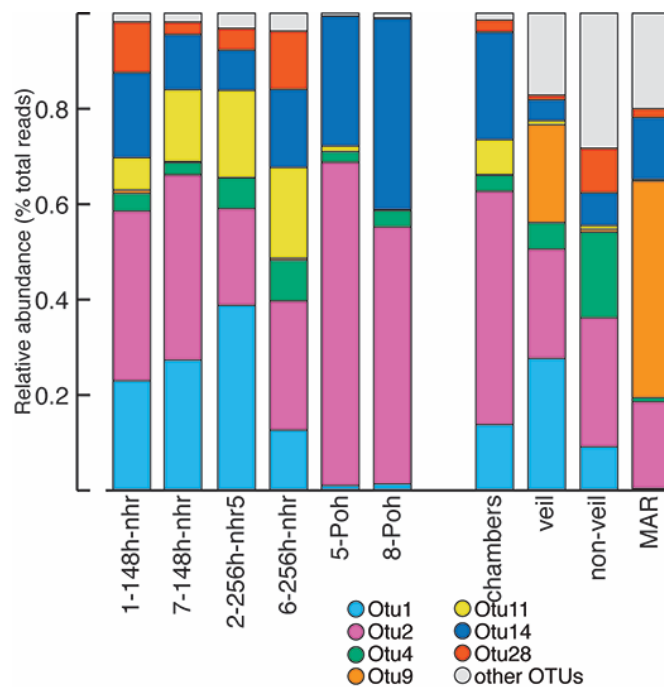
805

806

807
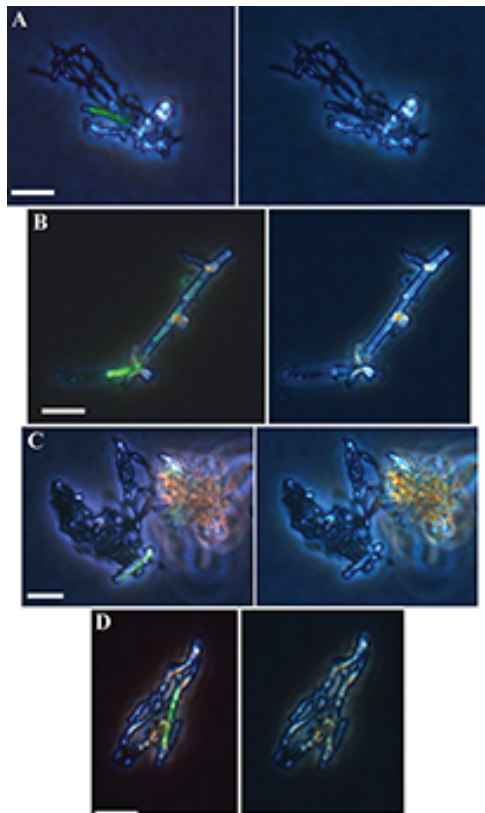
808
809
810
811

812   Fig. 6
813   Fig. 6. SSU rRNA amplicon community analysis of Zetaproteobacteria present in
814   chambers and iron mats. The left-hand set of columns show the relative abundance of
815   different ZetaOtus from the different incubation chambers. The right-hand columns
816   compare a sample that integrates all the chamber Zetaproteobacteria reads with either veil
817   or non-veil communities in mature Loihi iron mats, or iron mats from the Mid-Atlantic
818   Ridge (MAR). Note the presence of Otu11 in the chambers, and absence from the mats;
819   not the absence of Otu9 in the chambers, but presence in the mats. The data for the iron
820   mat comparisons are taken from Scott et al 2016.
821
822
823
824

825
826
827
828
829
830
831